COMMUNICATION

Fast oxygen ion migration in Cu–In–oxide bulk and its utilization for effective CO$_2$ conversion at lower temperature

Jun-Ichiro Makiura[a], Takuma Higo*[a], Yutaro Kurosawa[a], Kota Murakami[a], Shuhei Ogo[a], Hideaki Tsuneki[a], Yasushi Hashimoto[b], Yasushi Sato[b], Yasushi Sekine*[a]
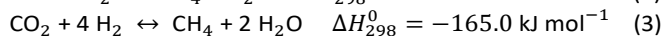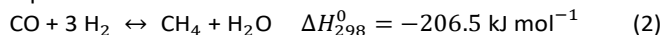
Efficient activation of CO$_2$ at low temperature was achieved by reverse water–gas shift *via* chemical looping (RWGS-CL) by virtue of fast oxygen ion migration in Cu–In–structured oxide, even at lower temperatures. Results show that novel Cu–In$_2$O$_3$ structured oxide can show a remarkably higher CO$_2$ splitting rate than ever reported. Various analyses revealed that RWGS-CL on Cu–In$_2$O$_3$ is derived from redox between Cu–In$_2$O$_3$ and Cu$_x$In$_y$ alloy. Key factors for high CO$_2$ splitting were fast migration of oxide ions in alloy and the preferential oxidation of the interface of alloy–In$_2$O$_3$ in the bulk of the particles. The findings reported herein can open up new avenues to achieve effective CO$_2$ conversion at lower temperatures.

Anthropogenic emissions of greenhouse gases (GHGs) are regarded as a cause of global warming, which is expected to lead to severe future climate change. Particularly, carbon dioxide (CO$_2$) derived from fossil fuels and industrial processes has long presented strong effects that continue to raise global mean temperatures [1,2]. Therefore, development of CO$_2$ capture and utilization (CCU) technologies [2-9] represents an urgent task for reducing CO$_2$ emissions into the atmosphere and for establishing a sustainable carbon cycle. Synthesis of fuels using electricity generation from renewable resources and using CO$_2$, most notably sun-to-fuel (STF)[5] and power-to-liquids[6] processes, has been proposed as a means of developing CCU. In fact, CO$_2$-based fuels are anticipated as a technology that can increasingly incorporate renewable energy into the mobility sector as an "e-fuel" [8,9]. For these fuel production technologies, the potential process route is a Fischer–Tropsch (FT) process using syngas, which includes hydrogen and carbon monoxide (CO) converted from captured CO$_2$ [2–4]. As a method of efficient conversion of CO$_2$ to CO through this process, reverse water–gas shift (RWGS) is a promising reaction that uses renewable H$_2$ [10,11].

Mallapragada *et al*. proposed that the STF route consisting of RWGS followed by the FT reaction has higher efficiency than that of other routes with direct CO$_2$ conversion by photosynthetic bacteria and biomass conversion [5]. The RWGS is an equilibrium limited reaction (equation 1) with an endothermic nature.

$$CO_2 + H_2 \leftrightarrow CO + H_2O \qquad \Delta H_{298}^0 = 42.1 \text{ kJ mol}^{-1} (1)$$

This reaction requires high reaction temperatures, separation of gas products to gain high conversion, and a suitable H$_2$/CO ratio syngas. Furthermore, conventional catalytic RWGS processes include side reactions, as presented in the following equations 2 and 3.

$$CO + 3 H_2 \leftrightarrow CH_4 + H_2O \qquad \Delta H_{298}^0 = -206.5 \text{ kJ mol}^{-1} \qquad (2)$$
$$CO_2 + 4 H_2 \leftrightarrow CH_4 + 2 H_2O \qquad \Delta H_{298}^0 = -165.0 \text{ kJ mol}^{-1} \qquad (3)$$

The CH$_4$ produced *via* these side reactions makes gas separation more complex. Additionally, it loses energy because of the exothermic reaction. One solution for this shortcoming is using chemical-looping reverse water–gas shift (RWGS-CL) [12,13]. The overall concept of solar-driven fuel (chemical) synthesis process with RWGS-CL is presented in Fig. 1. Through this process, CO$_2$ is converted to CO in two separate steps: reduction and re-oxidation of a metal oxide as an oxygen storage material (OSM). First, OSM is reduced by H$_2$ (reaction 4). Subsequently, the reduced OSM is re-oxidized by CO$_2$ to generate pure CO (reaction 5).
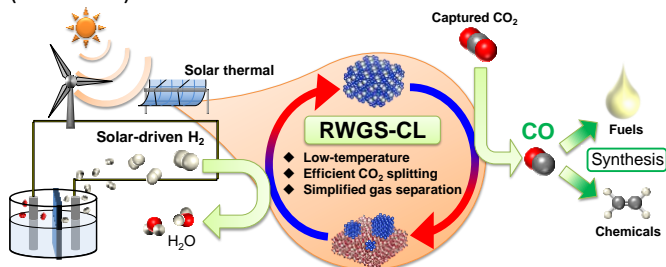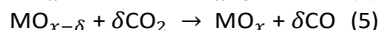

Fig. 1. Concept of solar-driven fuels and chemicals synthesis processes with RWGS-CL.

[a.] Department of Applied Chemistry, Waseda University, Tokyo 169-8555, Japan.
[b.] ENEOS, 1-1-2 Otemachi, Chiyoda, Tokyo 100 8162, Japan.
† *corresponding authors e-mail: t-higo@aoni.waseda.jp (Takuma Higo), ysekine@waseda.jp (Yasushi Sekine)

$$MO_x + \delta H_2 \rightarrow MO_{x-\delta} + \delta H_2O \quad (4)$$
$$MO_{x-\delta} + \delta CO_2 \rightarrow MO_x + \delta CO \quad (5)$$

Actually, RWGS-CL has benefits deriving from the absence of undesirable side reactions, which drives the equilibrium to CO production, and simplified gas separation, which leads to its improved energy efficiency. In fact, Wenzel *et al*. investigated solar-to-syngas efficiency for RWGS-CL processes and reported that the energy demand for separation is reduced by 77% compared to conventional RWGS processes [12]. In the RWGS-CL process, the development of OSM is an indispensable factor to make this process feasible. The rates of reduction and oxidation, CO yield, and stability are emphasized as key factors affecting OSM for the RWGS-CL cycles. Furthermore, the operation temperature is an important factor. Isothermal operation at lower temperatures is desired to reduce heat loss and to increase its feasibility [13]. In recent years, great effort has been put forth for the development of OSMs with high redox property for RWGS-CL [13–16]. This study has revealed that indium-based oxide can be a novel OSM material able to exhibit extremely high isothermal RWGS-CL performance at low temperatures (673–773 K). Particularly, the performance of Cu-modified In_2O_3 formed from $Cu_2In_2O_5$ as a parent material was found to be promising for this purpose. Characterizations of OSMs were conducted using powder X-ray diffraction (XRD), a field emission transmission electron microscope equipped with an energy-dispersive X-ray spectrometer (STEM-EDX), X-ray photoelectron spectroscopy (XPS), and *in-situ* X-ray absorption fine structure (XAFS) measurements.
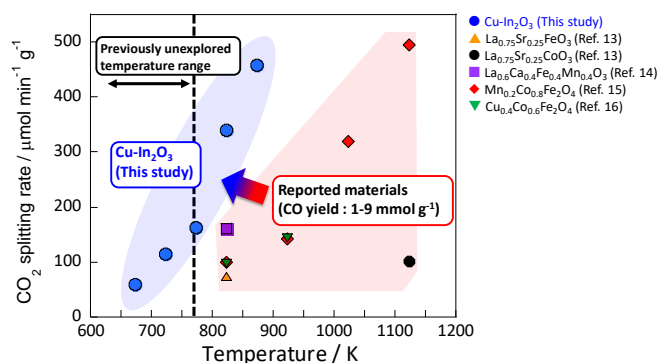

Fig. 2. Average CO_2 splitting rates on Cu–In mixed oxide (this study) and on various oxides in earlier reports.

Isothermal RWGS-CL performance

After applying various oxides for RWGS-CL, we found that Cu–In–mixed oxide has high potential for this RWGS-CL. The CO_2 splitting performance obtained in this study is presented in Fig. 2 and Table S1 along with results described in earlier reports of the literature. Compared to other perovskite-type oxides [13,14] and ferrite [15,16], which were reported earlier, Cu–In_2O_3 showed higher CO_2 splitting amounts and rates even at low temperatures such as 673–773 K. Among all the oxides, Cu–In_2O_3 derived from $Cu_2In_2O_5$ is the most promising material for low-temperature isothermal RWGS-CL. The cycle performance of isothermal RWGS-CL on $Cu_2In_2O_5$ at 773 K is presented in ESI Fig. S1. The reduction and oxidation (redox) amounts are defined as the moles of oxygen released or restored per gram of $Cu_2In_2O_5$. At the first cycle, $Cu_2In_2O_5$ showed reduction of
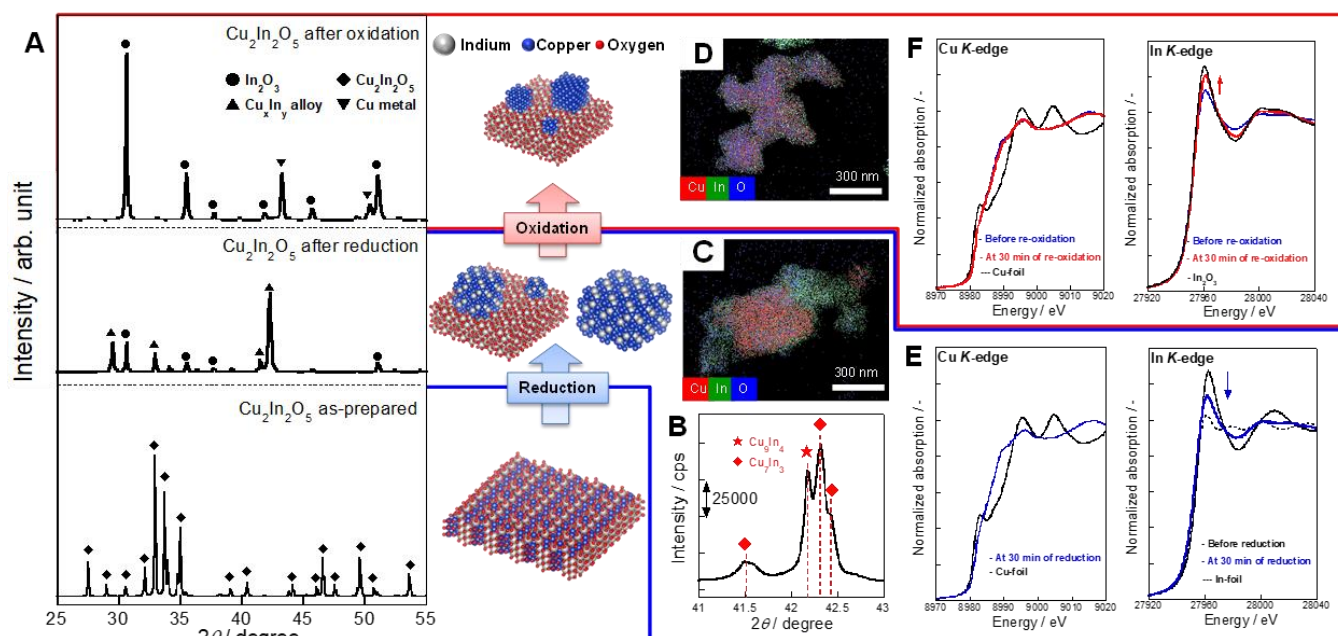

Fig. 3. Structural characterization for Cu–In_2O_3 derived from $Cu_2In_2O_5$ during each step of the RWGS-CL cycle. (A) XRD diffraction patterns of $Cu_2In_2O_5$ as prepared, after reduction, and after oxidation. (B) Main diffraction peaks for Cu_xIn_y alloy on the sample after reduction. EDX image of Cu–In_2O_3 after reduction (C) and re-oxidation (D) at 773 K (copper, red; indium, green; oxygen, blue). Cu and In *K*-edge XANES spectra of Cu–In_2O_3 during the reduction (E) and the re-oxidation (F).

9.50 mmol g^{-1} and re-oxidation of 4.82 mmol g^{-1}. Then, at cycles 2–5, the reduction and the oxidation amounts were, respectively, 5.06 ± 0.41 mmol g^{-1} and 4.80 ± 0.40 mmol g^{-1}. Excess reduction at the first cycle (= 4.68 mmol g^{-1}) was almost equivalent to the release of 2 mol oxygen atoms per mol of $Cu_2In_2O_5$. This finding suggests that $Cu_2In_2O_5$ has become Cu(0)–In_2O_3, which is confirmed later. Products of RWGS-CL were measured using a quadrupole mass spectrometer. The mass spectra of products are presented in ESI Fig. S2. The products at reduction and oxidation steps were identified respectively as H_2O (m/z = 18) and CO (m/z = 28) without production of other by-products. Results confirmed that RWGS-CL on Cu–In_2O_3 formed from $Cu_2In_2O_5$ is a selective CO_2 conversion to CO.

Structural characterization for this material was achieved using powder XRD, STEM-EDX, and *in-situ* XAFS measurements. The XRD patterns obtained from fresh and post-reaction samples are portrayed in Fig. 3A. The XRD pattern of the fresh sample showed the formation of $Cu_2In_2O_5$ with no impurity phase. The XRD pattern of the reduced sample exhibited diffraction peaks assigned to Cu_xIn_y alloy and In_2O_3. The main compositions of the alloy were Cu_7In_3 and Cu_9In_4 (Fig. 3B). Then, after the oxidation step, diffraction peaks of Cu_xIn_y alloy disappeared. Those of Cu metal and In_2O_3 were observed. STEM-EDX images are presented in Figs. 3C, D and ESI Fig. S3. The SEM micrographs taken of the reduced Cu–In_2O_3 (ESI Fig. S3A) show the presence of ca. 1 μm particles. The elemental composition of the particles was identified using EDX mapping (copper, red; indium, green; oxygen, blue). Results of EDX mapping of the sample after reduction (Fig. 3C and ESI Fig. S3A) show that indium is distributed evenly over the particle, whereas copper is localized; oxygen is scattered. These images indicate Cu_xIn_y alloy formation by reduction. For the re-oxidized sample, many particles with uniformly distributed copper, indium, and oxygen were observed as depicted in Fig. 3D and ESI Fig. S3B. Using image processing and analysis for these EDX images with Python (see ESI text and Fig. S4 for details), it was estimated that 84% of In exists as overlapping with Cu, and that 93% of Cu exists as overlapping with In. These results demonstrate that the fine matrix of Cu–In–O was formed in the re-oxidized particle. The Cu in re-oxidized particles was regarded as highly distributed on the surface, or incorporated into the In_2O_3 structure. As additional information, *in-situ* XAFS results are presented in Figs. 3E and 3F (see ESI text and Figs. S5–S7 for details). The sequential change of In *K*-edge XANES spectra indicates that the redox of In(III) $\leftrightarrows$ In(0) occurs during the RWGS-CL cycle. By contrast, Cu *K*-edge XANES spectrum, which only slightly changed during the RWGS-CL cycle, represented the formation of Cu–In alloy [17,18]. This structural information obtained from XRD, STEM-EDX, and XAFS measurements demonstrates that the RWGS-CL cycle on $Cu_2In_2O_5$, as a parent material, is based on the redox of indium with the formation and oxidation of Cu_xIn_y alloy. This material during RWGS-CL is designated hereinafter as Cu–In_2O_3.
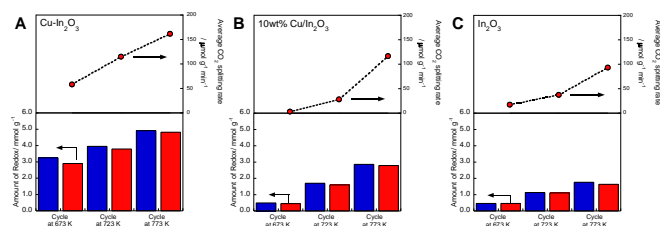

Fig. 4 Dependence of RWGS-CL performance of each oxide on the reaction temperature. Amounts of redox and average CO_2 splitting during re-oxidation step on Cu–In_2O_3 (A), 10wt% Cu/In_2O_3 (B), and In_2O_3 (C). Reduction was conducted in 10% H_2 atmosphere for 30 min; oxidation was conducted in 10% CO_2 atmosphere.

To elucidate the role of Cu in Cu–In_2O_3, we compared the performance of isothermal RWGS-CL as a function of temperature on Cu–In_2O_3 (derived from $Cu_2In_2O_5$), 10wt% Cu supported on In_2O_3 (10wt% Cu/In_2O_3) and pure In_2O_3 without Cu, as portrayed in Fig. 4. Results indicate that Cu–In_2O_3 is feasible for conducting RWGS-CL, even at 673 K. The performance at each temperature was much higher than that of 10wt% Cu/In_2O_3 and pure In_2O_3 without Cu. Actually, the amount of redox on 10wt% Cu/In_2O_3 was slightly higher than that of In_2O_3, although the CO_2 splitting rate was improved only slightly. Results of structural characterization for 10wt% Cu/In_2O_3 (ESI text and Figs. S8–S11 provide additional details) show that, because of the poor contact of Cu species with In_2O_3 surface, 10wt% Cu/In_2O_3 showed lower performance than that of Cu–In_2O_3 derived from $Cu_2In_2O_5$.

Kinetic investigations of oxides during the RWGS-CL cycle

Reduction step by H_2. Temperature-programmed reduction by H_2 (H_2-TPR) measurements, the results of which are presented in Fig. 5A, was done to investigate the reducibility of oxides. The ESI presents additional details.
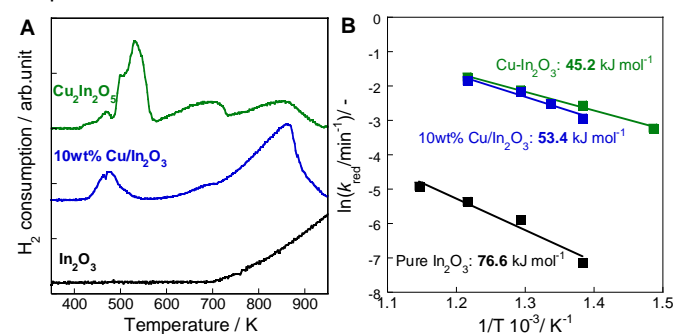

Fig. 5. Kinetic analysis for each oxide at the reduction step. (A) H_2-TPR profiles for Cu–In_2O_3 (derived from $Cu_2In_2O_5$), 10wt% Cu/In_2O_3 and In_2O_3. (B) Arrhenius plots for the reduction of Cu–In_2O_3 (derived from $Cu_2In_2O_5$), 10wt% Cu/In_2O_3 and In_2O_3.

For Cu-containing oxides (Cu–In_2O_3 and 10 wt% Cu/In_2O_3), the H_2-TPR profiles showed three notable reduction areas (ca. 400–550 K, 580–700 K, and 700–920 K). In the moderate temperature region of 580–700 K, the amount of reduction was

equivalent to about 26% of oxygen contained in $Cu_2In_2O_5$. Therefore, the reduction of In(III) with the formation of Cu_xIn_y alloy, the composition of which finally approached Cu_9In_4, was regarded as proceeding in this moderate temperature region. Regarding results of H_2-TPR measurements, results show that Cu species promote the reduction of indium oxide at low temperatures. To investigate more details of the mechanism, the kinetic model for the reduction of these oxides was verified using the method presented by Hancock and Sharp for the isothermal solid-state reaction [19–21]. The ESI text, Figs. S12–S15 and Tables S4–S6 present additional details. Kinetic models used for model fitting are shown in ESI Table S3. As a result of the investigations, the phase-boundary-controlled reaction models (R2 and R3 model) were found to be suitable to describe experimentally obtained data for all the oxides. These models are categorized to a classic shrinking core model in which the rate-controlling step is the surface chemical reaction [20,21]. The activation energy was investigated using the reaction rate constant k values obtained from the model fitting described above (ESI Table S7). Plots of ln (k) vs. $1/T$ (Arrhenius plot) for the three oxides are presented in Fig. 5B. The respective activation energies for Cu–In_2O_3 (45.2 kJ mol^{-1}) and 10 wt% Cu/In_2O_3 (53.4 kJ mol^{-1}) were much lower than that for In_2O_3 (76.6 kJ mol^{-1}), confirming that the Cu species supported on In_2O_3 decreased the activation barrier for reactions between the surfaces of In_2O_3 and H_2. The slight difference in the activation energy between Cu–In_2O_3 and 10 wt% Cu/In_2O_3 suggests that the effect of the Cu species on the reduction does not depend much on these morphologies.

Oxidation step by CO_2 for CO formation. Next, kinetic investigations were conducted of the oxidation step by CO_2 in the RWGS-CL cycle. The kinetic model for the oxidation of the oxide was also verified using the Hancock and Sharp method. As a consequence of the model fitting (details of which are presented in ESI Figs. S16–S19 and Tables S8–S10), the most suitable models were concluded to be a Zero-order model (R1 model) [19–21] for Cu–In_2O_3 and the nucleation model, known as the Avrami–Erofe'ev model (AE1 model), for the other two oxides [22–24]. Figure 6A presents the Arrhenius plot for the oxidation of these three oxides. The reaction rate constant k values obtained from model fitting are presented in Table S11. The activation energy for Cu–In_2O_3 is 50.7 kJ mol^{-1}, which is markedly lower than that for either of the other two oxides. As results of the model fitting show, the large difference in the activation energy is attributable to the different mechanisms of oxidation among these oxides. Considering that AE1 is suitable as a model for In_2O_3 and 10 wt% Cu/In_2O_3, results show that the overall oxidation of these two oxides is determined by the rate of formation and growth of the indium oxide nuclei. At the beginning of the reaction, the rate of oxidation is high because of random nucleation on the surface of the reduced oxide. However, as the nucleation and nuclei growth proceed, the rate of oxidation plummets because of the decrease of the reduced

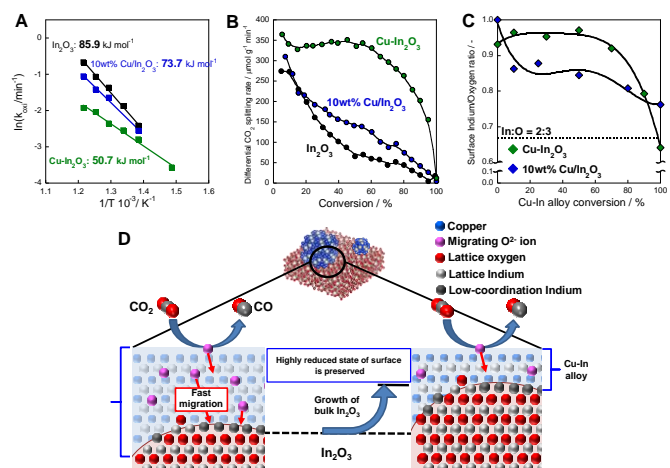surface. As a result, a long time is necessary to complete oxidation by CO_2.

Fig. 6. Kinetic analysis of each oxide at re-oxidation steps. (A) Arrhenius plots for the oxidation of Cu–In_2O_3 (derived from $Cu_2In_2O_5$), 10wt% Cu/In_2O_3 and In_2O_3. (B) Dependence of differential CO_2 splitting rate on conversion of oxides. (C) Surface In/O ratios on Cu–In_2O_3 and 10wt% Cu/In_2O_3 during re-oxidation step. (D) Presumed mechanism for CO_2 splitting on the reduced Cu–In_2O_3.

Figure 6B presents different rates of CO_2 splitting over these oxides during oxidation by CO_2. For all oxides, the degree of reduction before re-oxidation was fixed at 3.0 mmol g^{-1}. On In_2O_3 and 10 wt% Cu/In_2O_3, the CO_2 splitting rate decreased drastically with the progress of oxidation. The oxidation of Cu–In_2O_3 proceeded while maintaining a constant CO_2 splitting rate of about 340 μmol g^{-1} min^{-1} until conversion reached 60%. As a result, re-oxidation of the reduced Cu–In_2O_3 is completed twice as rapidly as those of the other two oxides. These results obtained from the kinetic investigation for Cu–In_2O_3 suggest that the amount of the active site for CO_2 splitting remains constant while oxidation is proceeding. Figure 6C shows the surface In/O ratio at each oxidation rate of the reduced Cu–In_2O_3 and 10wt% Cu/In_2O_3, as measured by XPS. The In/O ratio of the Cu–In_2O_3 surface remained above 0.9, even at the oxidation rate of 75%, which indicates that bulk oxidation proceeds preferentially while the surface remains in a highly reduced state. This particular CO_2 splitting mechanism of Cu–In_2O_3 is explainable as shown in Figure 6D. First, CO_2 splits on the surface of Cu–In alloy; the CO and oxide ion (O^{2-}) are generated. Subsequently, the O^{2-} migrates to the bulk of the particle. It presumably oxidizes the Cu–In alloy–In_2O_3 interface. As a result, the alloy surface, as the active site, remains in a highly reduced state. Rapid CO_2 splitting proceeds continuously.

Conclusion

As reported herein, Cu–In_2O_3 was synthesized. Then its performance for RWGS-CL was investigated at the low

temperatures of 673–773 K. Results of RWGS-CL cycle tests demonstrated that, even at low temperatures, Cu–In_2O_3 exhibited much higher CO_2 splitting performance than ever reported. Results of XRD, STEM-EDX, and *in-situ* XAFS measurements showed that the oxide has a structure of reduced Cu supported on In_2O_3 (Cu–In_2O_3) under the RWGS-CL condition, and showed that its redox property is based on Cu_xIn_y alloy formation and re-oxidation. In addition, because low performance was exhibited by pure In_2O_3 and Cu supported In_2O_3 that were prepared using an impregnation method, the structured state of Cu–In_2O_3 has extremely important roles for its high RWGS-CL performance. H_2-TPR and kinetic investigations revealed that Cu–In_2O_3 shows high reducibility, even at low temperatures. We concluded that Cu species promote the reaction of H_2 with the oxide surface. Results of kinetic investigations in the oxidation step indicate that the Cu_xIn_y particle surface conserved a highly reduced state, even in a re-oxidation condition, resulting in rapid completion of re-oxidation by CO_2. The interesting oxidation behavior is attributed to rapid O^{2-} migration from the surface to bulk of the Cu_xIn_y alloy and preferential oxidation of the interface of alloy–In_2O_3. The combination of high reducibility and the specific re-oxidation mechanism engenders the high performance found for RWGS-CL on Cu–In_2O_3.

Acknowledgements

Conflicts of interest

There are no conflicts to declare.

Notes and references

1   IPCC, www.ipcc.ch/site/assets/uploads/2018/02/SYR_AR5_FINAL_full.pdf.
2   S. J. Davis, K. Caldeira and H. D. Matthews, *Science* 2010, **329**, 1330-1333.
3   S. Perathoner and G. Centi, *ChemSusChem.* 2014, **7**, 1274-1282.
4   J. Artz, T. E. Müller and K. Thenert, *Chem. Rev.* 2018, **118**, 434-504.
5   D. S. Mallapragada, N. R. Singh, V. Curteanu and R. Agrawal, *Ind. Eng. Chem. Res.* 2013, **52**, 5136-5144.
6   F. V. Vázquez, J. Koponen, V. Ruuskanen, C. Bajamundi, A. Kosonen, P. Simell, J. Ahola, C. Frilund, J. Elfving, M. Reinikainen, N. Heikkinen, J. Kauppinen and P. Piermartini, *J. CO2 Util.* 2018, **28**, 235-246.
7   I. Dimitriou, P. G. Gutiérrez, R. H. Elder, R. M. C. Franca, A. Azapagic and R. W. K. Allen, *Energy Environ. Sci.* 2015, **8**, 1775-1789.
8   M. Romero and A. Steinfeld, *Energy Environ. Sci.* 2012, **5**, 9234-9245.
9   P. Kaiser, R. B. Unde, C. Kern and A. Jess, *Chem. Ing. Tech.* 2013, **85**, 489-499.
10 Y. A. Daza and J. N. Kuhn, *RSC Adv.* 2016, **6**, 49675-49691.
11 K. Oshima, T. Shinagawa, Y. Nogami, R. Manabe, S. Ogo and Y. Sekine, *Catal. Today* 2016, **232**, 27-32.
12 M. Wenzel, L. Rihko-Struckmann and K. Sundmacher, *AIChE J.* 2015, **61**, 2-22.
13 Y. A. Daza, D. Maiti, R. A. Kent, V. R. Bhethanabotla and J. N. Kuhn, *Catal. Today* 2015, **258**, 691-698.
14 D. Maiti, B. J. Hare, Y. A. Daza, A. E. Ramos, J. N. Kuhn and V. R. Bhethanabotla, *Energy Environ. Sci.* 2018, **11**, 648-659.
15 L. Ma, Y. Qiu, M. Li, D. Cui, S. Zhang, D. Zheng and R. Xao, *Ind. Eng. Chem. Res.* 2020, **59**, 6924-6930.
16 Y. Qiu, L. Ma, D. Zeng, M. Li, D. Cui, Y. Lv, S. Zhang and R. Xiao, *J. Energy Chem.* 2020, **46**, 123-132.
17 M. G. Kim, S. Sim and J. Cho, *Adv. Mater.* 2010, **22**, 5154-5158.
18 W.-R. Lee, M. G. Kim, J.-R. Choi, J.-I. Park, S. J. Ko, S. J. Oh and J. Cheon, *J. Am. Chem. Soc.* 2005, **127**, 16090-16097.
19 J. D. Hancock and J. H. Sharp, *J. Am. Ceram. Soc.* 1972, **55**, 74-77.
20 K. Piotrowski, K. Mondal, H. Lorethova, L. Stonawski, T. Szymański and T. Wiltowski, *Int. J. Hydrogen Energy* 2005, **30**, 1543-1554.
21 Z. Zhou, L. Han and G. M. Bollas, *Int. J. Hydrogen Energy* 2014, **39**, 8535-8556.
22 M. Avrami, *J. Chem. Phys.* 1939, **7**, 1103-1112.
23 M. Avrami, *J. Chem. Phys.* 1940, **8**, 212-224.
24 M. Avrami, *J. Chem. Phys.* 1941, **9**, 177-184.